

MDA GAN: Adversarial-Learning-based 3-D Seismic Data Interpolation and Reconstruction for Complex Missing

Yimin Dou, Kewen Li, Hongjie Duan, Timing Li, Lin Dong, Zongchao Huang

Abstract—The interpolation and reconstruction of missing traces is a crucial step in seismic data processing, moreover it is also a highly ill-posed problem, especially for complex cases such as high-ratio random discrete missing, continuous missing and missing in fault-rich or salt body surveys. These complex cases are rarely mentioned in current sparse or low-rank prior-based and deep learning-based approaches. To cope with complex missing cases, we propose Multi-Dimensional Adversarial GAN (MDA GAN), a novel 3-D GAN framework. It employs three discriminators to ensure the consistency of the reconstructed data with the original data distribution in each dimension. The feature splicing module (FSM) is designed and embedded into the generator of this framework, which automatically splices the features of the unmissing part with those of the reconstructed part (missing part), thus fully preserving the information of the unmissing part. To prevent pixel distortion in the seismic data caused by the adversarial learning process, we propose a new reconstruction loss Tanh Cross Entropy (TCE) loss to provide smoother gradients. We experimentally verified the effectiveness of the individual components of the study and then tested the method on multiple publicly available data. The method achieves reasonable reconstructions for up to 95% of random discrete missing, 100 traces of continuous missing and more complex hybrid missing. In surveys of fault-rich and salt bodies, the method can achieve promising reconstructions with up to 75% missing in each of the three directions (98.2% in total).

Index Terms—GAN, adversarial learning, seismic data interpolation, seismic data reconstruction, seismic complex missing

I. INTRODUCTION

Complete seismic data are often difficult to acquire due to various constraints such as economic, physical, and other factors. Reconstructing missing seismic data is a critical and challenging task.

There are currently two major types of methods for interpolation and reconstruction of seismic data, theory-driven and data-driven [1], [2]. Theory-driven uses mathematical and physical methods, such as fluctuation equations, sparse representations and low-order [3]–[10]. These methods are

based on theoretical assumptions, which are difficult to get promising results in the field with complex seismic data and are computationally expensive without better hardware acceleration.

Data driven employing machine learning or deep learning, there are generally two types of methods, Auto-Encoder (AE) and Generative Adversarial Neural Networks (GAN). AE-based methods include using AE [11], CAE [12], UNet [1] and ResNet [13], etc. These methods are essentially regression methods using neural networks, which have promising results in random discontinuous 2-D deficiencies, but less effective for continuous missing. He et al. used a multi-stage UNet to step through the interpolation of consecutive missing [14]. Although the method is able to repair continuous missing, the seismic data are encoded and decoded multiple times causing massive pixel distortion and blurring. Li et al. used Coordinate Attention UNet to interpolate the continuous missing [15]. Yu et al. used attention mechanism and hybrid loss to achieve reconstruction of missing 2-D continuous seismic traces [2]. The above methods all achieve promising interpolation for 2-D continuous missing with an upper limit of 38 traces of continuous missing, and these papers have limited discussion of more difficult cases. The case of field data is more complex, such as high-ratio random discrete missing, continuous missing and missing in rich fault or salt body surveys or 3-D cases. DTAE proposed by Qian et al. is the first to discuss data-driven interpolation methods in the 3-D case [16], but its performance is weak for large scale or continuous missing.

Additional to this are GAN-based methods, which have been less studied. GAN is based on adversarial learning, which essentially gives the most reasonable hypothesis given the existing prior conditions. Oliveira achieved interpolation and reconstruction of Netherlands Offshore F3 seismic data via cGANs [17]. He used L_1 as the reconstruction loss for 2-D interpolation, and the results have clear splicing traces. Wei et al. changed the adversarial loss to Wasserstein loss based on cGAN and achieved 2-D interpolation of up to 35 consecutive seismic traces. [18]. Kaur et al. used GAN and CycleGAN to interpolate 2-D synthetic seismic data [19], [20]. The above GAN-based methods do not target seismic data for improvement and only fix simple missing cases, which do not take advantage of GAN. In addition, the current GAN-based methods are for 2-D data, and it is difficult to achieve consistency and coherence in slicing in all directions when handling 3-D data by interpolating the results from 2-D networks.

The corresponding author is Kewen Li. likw@upc.edu.cn

Yimin Dou, Kewen Li, Zongchao Huang, College of computer science and technology, China University of Petroleum (East China) Qingdao, China.

Timing Li, College of Intelligence and Computing, Tianjin University Tianjin, China.

Hongjie Duan, Shengli Oilfield Company, SINOPEC Dongying, China.

Lin Dong, Center on Frontiers of Computing Studies, Peking University Beijing, China

This work was supported by grants from the National Natural Science Foundation of China (Major Program, No.51991365), and the Natural Science Foundation of Shandong Province, China (ZR2021MF082).

The current approach has achieved promising reconstructions for some simple missing cases, i.e. up to 50% random discrete missing ([16] etc.) and up to 38 consecutive missing traces ([2] etc.). However there are still many surveys where the situation is more difficult than these. Therefore, this study presents the Multi-Dimensional Adversarial GAN (MDA GAN) to interpolate 3-D complex continuous or discrete or more severe missing. Handling missing 3-D data requires ensuring that the reconstructed data needs to be consistent with the original distribution in both the 3-D view (3-D domain) and the sliced view (2-D domain), which is especially important in the case of complex missingness. We therefore propose a novel GAN framework for seismic data reconstruction, employing three discriminators to guarantee its correctness in both domains. This framework consists of a 3-D generator, a 3-D discriminator and two 2-D discriminators, where the generator uses the structure that propagates two scale features in parallel and the discriminators all use the encoder structure.

Data restoration via neural networks can result in differences between the unmissing part of the original (input) and the same part of the result (output). Some existing studies stitch the input and output by masks [21]–[24]. All the missing seismic traces or regions need to be manually marked beforehand if masks are applied in the reconstruction of seismic data, which requires a great deal of effort. Accordingly, we designed the Feature Splicing Module (FSM), which expresses explicitly the splicing process between the original features and the generated features, making the network complete the end-to-end generation and splicing process. By outputting the FSM feature map, we find that the module makes the network auto-generate the mask during the inference process. Thus, the output fully retains the features of the missing part of the input data, and the splicing process can be done automatically without manually marking the missing seismic traces.

To ensure the stability of the training of GANs, the last layer of the generator network often needs to use the Tanh activation function [25]–[29], and for seismic interpolation it is necessary to reconstruct the seismic data, the traditional reconstruction loss uses L_1 and L_2 [26]–[29], and the gradient of these two losses under the Tanh activation function is not smooth, especially for seismic data, the amplitude changes are large and high frequency, and the generated seismic data is easy to distortion [17]. Based on this, we propose a pixel reconstruction loss Tanh Cross-Entropy (TCE) which uses the residuals of the model estimate and ground truth under Tanh as the gradient, thus making the gradient smoother.

Overall, in this study to cope with more complex 3-D seismic missing cases we present a novel GAN framework, MDA GAN, which uses three discriminators to guarantee the consistency of two domains, thus enabling high quality interpolation even in most complex missing cases. FSM is designed to complete the end-to-end data generation and splicing process. Finally, the TCE reconstruction loss is also proposed to enable the training process to provide smoother gradients and ensure pixel-less distortion of the generated data.

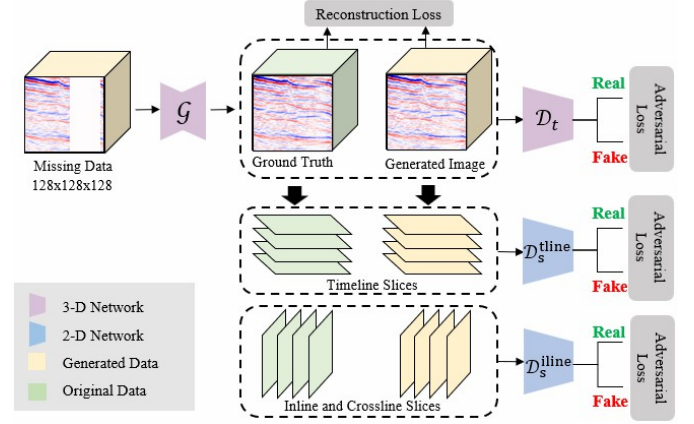


Fig. 1. Our framework consists of one 3-D generator, one 3-D discriminator and two 2-D discriminators. We employ a reconstruction loss to enable the generator to maintain the original prior, and an adversarial loss to learn the distribution $p(\mathbf{I}_c|\mathbf{I}_m)$ of the data under this prior. The generator yields a complete seismic cuboid, which consists of two parts, \mathbf{I}'_m and \mathbf{I}_c , where \mathbf{I}'_m is the reconstructed \mathbf{I}_m , \mathbf{I}_c is the generated interpolated data.

II. APPROACH

In this section, we first introduce the baseline framework of MDA GAN, then illustrate the structure of FSM and how it is embedded and functions in the generator, and finally discuss the seismic voxel (pixel) level reconstruction loss Tanh Cross Entropy Loss (TCE) and analyze its training gradient to illustrate the advancement of the method.

A. Baseline Framework

Interpolation of seismic images where missing data \mathbf{I}_m (input) is known and on the basis of this a priori, the patch data \mathbf{I}_c (output) is found so that it is as close as possible to the original data \mathbf{I}_g (target).

The regression method can obtain promising results for simple cases (well posed problem or near well posed problem). However, for cases requiring complex interpolation, i.e., where missing information occurs and it does not have a reasonable way to estimate the missing region \mathbf{I}_c , the regression method becomes stretched to the limit.

GAN are proposed by Goodfellow et al. [30]. It consists of a generator network \mathcal{G}_{θ_G} and a discriminator network \mathcal{D}_{θ_D} , where the task of the generator is to yield images $x \in \mathcal{R}^{N_w \times N_h}$ with a latent noise prior vector, $z \in \mathcal{R}^d$ as input z is sampled from a known distribution, i.e. latent vector $z, z \sim \mathcal{U}[-1, 1]^d$ [30]. The task of the discriminator is to distinguish real images from generated ones. The generator and the discriminator play a zero-sum game in which the two networks learn from each other and the data obtained by the generator becomes increasingly close to the real data, so that the desired data can be generated. The objective function of GANs can be expressed by the equation (1).

$$\begin{aligned} \max_{\mathcal{G}_{\theta_G}} \min_{\mathcal{D}_{\theta_D}} V(\mathcal{G}_{\theta_G}, \mathcal{D}_{\theta_D}) = \\ \mathbb{E}_{x \sim p_{data}(x)} [\log \mathcal{D}_{\theta_D}(x)] + \mathbb{E}_{z \sim p_z(x)} [1 - \log \mathcal{D}_{\theta_D}(\mathcal{G}_{\theta_G}(z))] \end{aligned} \quad (1)$$

General GAN focus on learning a data distribution, hoping that the learned distribution is similar to the real data. And we need the GANs that can be used to fill the missing region \mathbf{I}_c . Each output prediction should be based on the prior of the input data \mathbf{I}_m , this make the data distribution be a conditional distribution i.e. $p(\mathbf{I}_c|\mathbf{I}_m)$.

In MDA GAN, we construct the latent vector z based on the missing input data $P_{\theta_z}(\mathbf{I}_m)$. z contains the prior information of \mathbf{I}_m , and the generator outputs fake data based on z . To preserve the prior of z requires supervised learning of the data generated by the generator using reconstruction loss (generally L_1 or L_2), and the generator is also supervised adversarial loss (equation 2).

$$\mathcal{L}_G = \log(1 - \mathcal{D}_{\theta_D}(\mathcal{G}'_{\theta_G}(P_{\theta_z}(\mathbf{I}_m)))) \quad (2)$$

Neural networks can approximate any function or distribution, so in practice, it is possible to make $\mathcal{G}'_{\theta_G}(P_{\theta_z}(\mathbf{I}_m)) = \mathcal{G}_{\theta_G}(\mathbf{I}_m)$, so equation (2) becomes (3).

$$\mathcal{L}_G = \log(1 - \mathcal{D}_{\theta_D}(\mathcal{G}_{\theta_G}(\mathbf{I}_m))) \quad (3)$$

Coping with missing 3-D data requires ensuring that the reconstructed data needs to be consistent with the original distribution in both the 3-D domain and the 2-D domain, which is especially important in the case of complex missing data. Consequently we use two types of discriminators (2-D and 3-D networks, i.e. $\mathcal{D}_{\theta_D}^m$ and $\mathcal{D}_{\theta_D}^t$) to supervise the two domains separately in order to make the generated data consistent with the original distribution in both 2-D and 3-D domains. In particular, anisotropy is common for 3-D seismic data. Seismic anisotropy is usually defined as the difference between velocities parallel to the ground level and velocities perpendicular to the ground level. Therefore, in the 2-D domain, we use two discriminators for lateral and longitudinal velocities, i.e., inline and crossline share the same discriminator $\mathcal{D}_{\theta_D}^m$, and timeline uses a separate discriminator $\mathcal{D}_{\theta_D}^t$. Correspondingly, the generator is supervised by three adversarial losses and one reconfiguration loss, which is expressed in equation 4.

$$\mathcal{L}_G = \mathcal{L}_{G^t} + \mathcal{L}_{G_{\text{xline}}^m} + \mathcal{L}_{G_{\text{tline}}^m} + \lambda \mathcal{L}_{\text{rec}} \quad (4)$$

where λ is a scaling factor to adjust the reconstruction loss to the same order of magnitude as the adversarial loss. For reconstructing high-quality seismic data, our approach employs adversarial learning in multiple dimensions, hence the term Multi-Dimensional Adversarial (MDA) GAN.

Each discriminator determines the authenticity of the generated tensor or matrix, using the cross-entropy loss for supervision, equation 5.

$$\mathcal{L}_D = \frac{1}{2} \log(1 - \mathcal{D}_{\theta_D}(\mathbf{I}_g)) + \frac{1}{2} \log(-\mathcal{D}_{\theta_D}(\mathcal{G}_{\theta_G}(\mathbf{I}_m))) \quad (5)$$

The overall framework of MDA GAN is shown in Fig.1.

B. Generator

1) *Architecture*: Traditional generators normally take the form of concatenating high-resolution features with low-resolution features, i.e., encoder-decoder structures, and related models are available for various vision tasks [21]–[24].

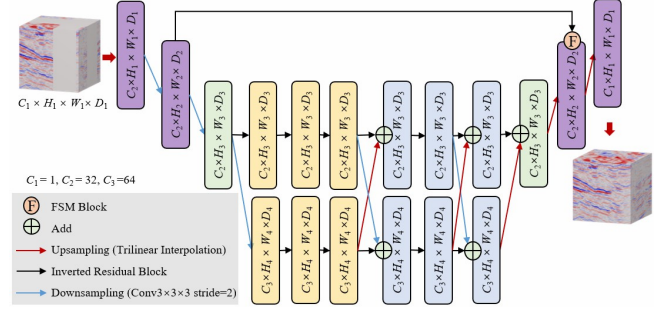


Fig. 2. The generator architecture. Instead of using the encode-and-decode structure commonly used by generators, we propagate the features on both scales in parallel.

However, such methods downsample the features several times and returns the original resolution via the decoder, which causes the loss of information, while the process of restoring the resolution requires plenty of parameters and eats up many video memory resources. The new model design idea of parallel propagation of high resolution with low resolution was proposed by Wang and Sun et al. [31], [32], and our previous work demonstrated that this structured network can achieve higher performance with few hardware resources [33]. We designed the generator based on this structure, using fewer computational resources to ensure the generation of high-quality data.

Resblock [34] is selected as the base block of the generator. The network is downsampled only twice, and then a low-resolution branch is added for parallel propagation, which is structured as shown in Fig. 2. Because the network keeps the high-resolution features, we don't need an excessive width and depth to ensure that the network recovers from the low resolution, so we use fewer parameters and save much bandwidth.

2) *Feature Splicing Module*: To adequately preserve the unmissing information of the input data \mathbf{I}_m , many works perform splicing of \mathbf{I}_m with \mathbf{I}_c via mask, and the splicing process is expressed as equation 6.

$$\mathbf{I}_g \approx \mathbf{I}'_g = (1 - \mathcal{M}) \times \mathbf{I}_c + \mathcal{M} \times \mathbf{I}_m \quad (6)$$

Where \mathcal{M} is mask, which is a matrix of the same size as the inputs, with 0 indicating missing data and the opposite with 1. However, for seismic data, it is difficult to obtain the mask and requires manual marking of missing regions, especially for 3-D data, which can consume a tremendous effort. Not splicing will cause the resulting $(1 - \mathcal{M}) \times \mathbf{I}_c$ to differ from the original data $(1 - \mathcal{M}) \times \mathbf{I}_g$ as shown in Fig. 7 (d-1). We wanna find a solution to replace the role of \mathcal{M} and to form end-to-end training and inference.

For this purpose, we presented FSM. Our approach is to splice the low-level features of the network (representing the original non-missing part) with the high-level features (representing the generated part) so that the network automatically completes this process, and then reconstructs the spliced features to output the result. The existing work such as UNet [23] which concatenates the high level and bottom level features and then fuses them using convolution does

not express the splicing process explicitly, and in the fusion process, the missing and unmissing of the bottom level features but with have the same weight, which can lead to distortion or blurring of the generated image.

The module can be represented by the following equation (7, 8, 9).

$$\mathcal{F}^{\text{branch}} = \mathbf{F}^{\text{cat}}(\mathcal{F}^l, \mathcal{F}^h) \quad (7)$$

$$\mathcal{W}_m = \sigma(\mathbf{F}^{\text{conv}}(\mathbf{F}^{\text{conv}}(\mathcal{F}^{\text{branch}}, 1, 1, 2C_1, C_1), 1, 1, C_1, 2C_1)) \quad (8)$$

$$\mathcal{F}^{\text{spl}} = \mathbf{F}^{\text{conv}}(\mathcal{W}_m \odot \mathcal{F}^{\text{branch}}, 1, 1, 2C_1, C_1) \quad (9)$$

In equation (7) the features are concatenated with the high-level feature \mathcal{F}^h and the low-level feature \mathcal{F}^l to obtain $\mathcal{F}^{\text{branch}}$, and the channel after concatenation is changed from C_1 to $2 \times C_1$. \mathcal{F}^l uses the features after the first convolution and \mathcal{F}^h uses the features before the last residual block, so they both keep the original feature resolution. \mathcal{F}^l has not been downsampled and convolved multiple times, so it retains all the information of the original data, and \mathcal{F}^h has been filled with the missing parts after the generator network.

We want to express the splicing process of the features explicitly, so that the network automatically expresses equation 6, we compress and weight $\mathcal{F}^{\text{branch}}$ by a 1×1 convolution, then recover it to the original channel and restrict its value domain to $[0, 1]$ by the sigmoid ($\sigma(x_i) = \frac{1}{1+\exp(-x_i)}$) activation function to obtain \mathcal{W}_m , the above process is represented by equation 8.

After equation (9), the FSM can be updated via standard backpropagation, and our experiments show that the module is able to converge \mathcal{W}_m so that it generates a feature mask that resembles \mathcal{M} and applies it to the splicing of features. The entire process can be represented in Fig. 3.

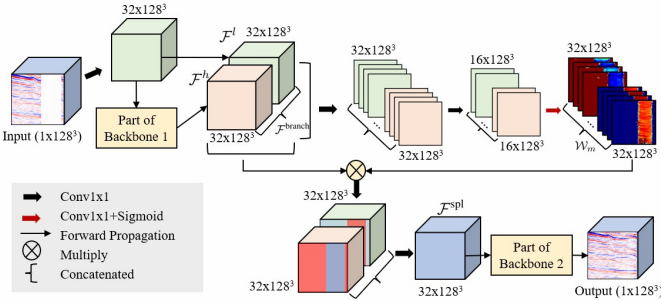


Fig. 3. The FSM is embedded into the generator network. Since FSM processes unsampled features, thus the whole module adopts 1×1 convolution to save computational expenses, and it selects the spatial response of the splicing by obtaining the high-dimensional mapping of $\mathcal{F}^{\text{branch}}$ to automate the splicing process.

We visualized \mathcal{W}_m , which has channel $2C_1$ and has two components, \mathcal{W}_l (C_1 channels) and \mathcal{W}_h (C_1 channels), with \mathcal{W}_l corresponding to the \mathcal{F}_l part of the $\mathcal{F}^{\text{branch}}$ and \mathcal{W}_h corresponding to the \mathcal{F}_h part, and Fig. 4 shows the weights of \mathcal{W}_m with different patterns of input.

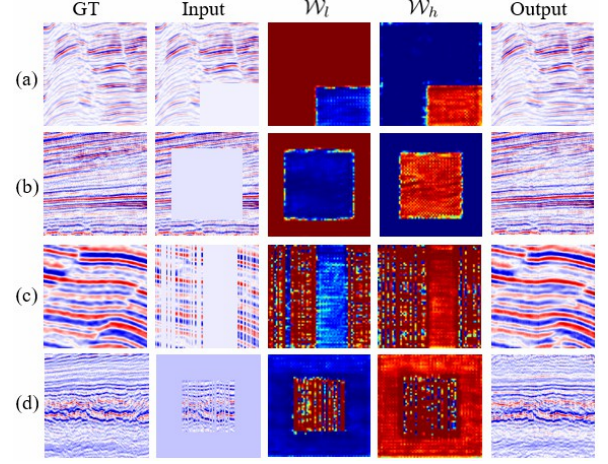


Fig. 4. The figure is shown as 2-D slices of 128^2 in 3-D volumes of 128^3 , displaying the missing of the five modes. The FSM generates mask-like heatmaps without any mask supervision information.

The approach don't input any supervised information about mask (\mathcal{M}), but the network still adaptively generates a mask-like heatmap. The supervision of the reconstruction loss and the FSM force \mathcal{W}_m to automatically form semantic weights, and during continuous training, the network gradually learns which parts of the features should be extracted and retained.

C. Discriminator

The discriminator network uses the structure of a standard encoder. The discriminator consists of five convolutional layers, and each layer employs the LeakyReLU [25] activation function, and also incorporates the spectral normalization [35] to stabilize the training of the GANs.

D. Tanh Cross Entropy Loss

Most of the current reconstruction losses are based on L_1 and L_2 [26]–[29], where L_1 provides stable gradients and L_2 ensures that the neural network has a unique solution, but both loss functions have the common disadvantage of unsmoothed gradients in GANs. Generator networks generally use Tanh as the final activation layer to keep the network's value domain at $[-1, 1]$, while ensuring training stability [25]. Next we derive the gradient expressions for L_1 and L_2 under the Tanh activation function.

First we analyze the gradient form of the L_1 loss.

$$\mathcal{L}_{L_1} = \frac{1}{N_w \times N_h \times N_d} \sum_i \sum_j \sum_k |y_{i,j,k} - \hat{y}_{i,j,k}| \quad (10)$$

$$\hat{y}_i = \text{Tanh}(\hat{x}) = \frac{e^{\hat{x}} - e^{-\hat{x}}}{e^{\hat{x}} + e^{-\hat{x}}}, \frac{d\hat{y}}{d\hat{x}} = 1 - \hat{y}^2 \quad (11)$$

$$\begin{aligned} \frac{\partial \mathcal{L}_{L_1}(y, \hat{y})}{\partial \hat{x}_t} &= \frac{\partial \mathcal{L}_{L_1}(y, \hat{y})}{\partial \hat{y}_t} \cdot \frac{\partial \hat{y}_t}{\partial \hat{x}_t} \\ &= \begin{cases} 1 - \hat{y}_t^2 & \text{if } y_t - \hat{y}_t \geq 0 \\ \hat{y}_t^2 - 1 & \text{if } y_t - \hat{y}_t < 0 \end{cases} \end{aligned} \quad (12)$$

The gradient amplitude of the L_1 loss can thus be seen to be related to the square of the predicted value, while the residual $(y - \hat{y})$ between the predicted value (\hat{y}) and the Ground Truth (GT, y) only controls the direction of the gradient. We will denote the residuals by ε .

$$\mathcal{L}_{L_2} = \frac{1}{N_w \times N_h \times N_d} \sum_i \sum_j \sum_k \|y_{i,j,k} - \hat{y}_{i,j,k}\|_2^2 \quad (13)$$

$$\begin{aligned} \frac{\partial \mathcal{L}_{L_1}(y, \hat{y})}{\partial \hat{x}_t} &= \frac{\partial \mathcal{L}_{L_1}(y, \hat{y})}{\partial \hat{y}_t} \cdot \frac{\partial \hat{y}_t}{\partial \hat{x}_t} \\ &= 2(y_t - \hat{y}_t)(1 - \hat{y}_t^2) \end{aligned} \quad (14)$$

The gradient of the L_2 loss is still correlated with the predicted value squared, and the ε control the direction and amplitude of the gradient. The ideal form of the gradient should be positively correlated with ε , whereas from Equations (12) and (14), the L_1 and L_2 gradients and residuals do not satisfy this condition and therefore they result in an unsmoothed gradient when trained.

We wanted to use ε directly as a gradient, so that voxels with larger differences in values would give greater feedback, and voxels with smaller differences would give smaller feedback.

Then the loss function we expect can be expressed by the equation (15).

$$\begin{aligned} \mathcal{L}_{TCE}(y_t, \hat{y}_t) &= \int \varepsilon \cdot \frac{\partial \hat{x}_t}{\partial \hat{y}_t} d\hat{x}_t = \int \frac{y_t - \hat{y}_t}{1 - \hat{y}_t^2} d\hat{x}_t \\ &= -y_t \left(\frac{\log|\hat{y}_t + 1|}{2} - \frac{\log|\hat{y}_t - 1|}{2} \right) \\ &\quad - \frac{1}{2} \log|1 - \hat{y}_t^2| + \log 2 + C' \\ &= - \left[\left(\frac{1 + y_t}{2} \right) \log \left(\frac{1 + \hat{y}_t}{2} \right) + \left(\frac{1 - y_t}{2} \right) \log \left(\frac{1 - \hat{y}_t}{2} \right) \right] \end{aligned} \quad (15)$$

The losses of all voxels should be averaged during training, so that the loss expression is (16).

$$\begin{aligned} \mathcal{L}_{TCE}(y, \hat{y}) &= \frac{1}{N_w \times N_h \times N_d} \sum_i \sum_j \sum_k \\ &\quad \left[\left(\frac{1 + y_{i,j,k}}{2} \right) \log \left(\frac{1 + \hat{y}_{i,j,k}}{2} \right) + \left(\frac{1 - y_{i,j,k}}{2} \right) \log \left(\frac{1 - \hat{y}_{i,j,k}}{2} \right) \right] \end{aligned} \quad (16)$$

Its form is similar to cross-entropy, so we named it Tanh Cross-Entropy (TCE). This loss causes the gradient at training as in equation (17).

$$\frac{\partial \mathcal{L}_{TCE}(y, \hat{y})}{\partial \hat{x}_t} = y_t - \hat{y}_t = \varepsilon \quad (17)$$

The gradient of TCE under Tanh is equal to the residual of GT and the predicted value, which provides the smoothest gradient that reasonably reflects the distance between the true distribution and the model distribution.

E. Training

The over-arching training framework follows the Fig. 1. The optimizer uses Adam [36]. In general, the training of the discriminator should be ahead of the generator, which is more conducive to producing high-quality data. We use the TTUR strategy for training [37], setting the learning rate of discriminators $\eta_d = 0.0004$ and the generator $\eta_g = 0.0001$, finally alternating the training of the generator and discriminators.

III. EXPERIMENTS

We set up four groups of experiments: Group-1, Group-2, Group-3, and Group-4 to verify the effectiveness of each component and test the performance of each method. The settings of the four groups of experiments are shown in Table I.

TABLE I
EXPERIMENTAL GROUPING

	Method	Explain
Group-1	UNet	UNet-based regression
Group-2	MDA Reg	Regression by generators only
Group-3	MDA GAN (L_1)	without TCE, with L_1 loss
Group-4	MDA GAN	Our method

Among them, Group-2 (MDA Reg) is a regression method using the generator of MDA GAN as the backbone. The comparison between Group-2 and Group-4 can verify the effectiveness of multidimensional adversarial learning. Group-2 is trained in the same way as Group-1 (UNet), but the backbone is different, which can test the performance of our generator by comparing the performance. Group-3 (MDA GAN (L_1)) does not use TCE to reconstruct the loss, but uses L_1 loss, which can be used to verify the validity of TCE. It is important to note that the last layer of the network output in the regression task does not need to go through the activation function, so its training by L_1 loss.

The experiments used data from Sinopec and 75% of the New Zealand Openake 3-D as the training set and 25% as the validation set. We conduct sliding sampling with a stride of 64 via a window with $128 \times 128 \times 128$, i.e., the training input data size is 128^3 , and randomly remove 30 – 99% of these traces as input data. The whole process don't require manual labeling. Training was performed on two NVIDIA Tesla P100 GPUs and accelerated via NVIDIA Apex, the batch size is 4 and 500,000 iterations.

A. Random Discrete Missing

We first test the performance of the three methods under discrete and random missing cases. Fig. 5 displays the result of the four groups on a cuboid of $256 \times 160 \times 128$ in Parihaka-3-D. The 5.(a) shows that at 50% missing, all four methods work well and there is no significant difference in the interpolation results. At 75% missing, the regression-based methods are a bit less powerful, as evident from the interpolation traces in the timeline slices in 5.(b-3) and 5.(b-4). When the missing increases to 90%, regression-based methods shows a large-scale void, and 5.(c-4) completes the reconstruction, but its

performance is significantly worse than that of 5.(c-5) and (c-6). At 95% missing, the regression method had failed and only the MDA GAN completed the reconstruction, multi-dimensional adversarial learning allows the network's output to remain consistent with the original distribution across dimensions, allowing it to output reasonable results even with a very high proportion of missingness. Group-4 using TCE performed better than Group-3 using L_1 , and the reconstruction results using L_1 loss showed distortion of some voxels when there is a massive missing, it is demonstrated that the smoother gradients provided by TCE can make the reconstruction results more continuous and reliable.

Table II shows the results of the experimental quantification using the Structural Similarity (SSIM) and Peak Signal to Noise Ratio (PSNR) metrics. Zhou et al. explored in detail SSIM and PSNR [38], where PSNR reflects the pixel differences between the interpolated results and Ground Truth (GT), while SSIM is more in line with the human visual system, which reflects the structural similarity of the images. The table shows that the quantifiers of all four methods decrease as the missing rate increases, but the MDA GAN decreases significantly less than the other methods.

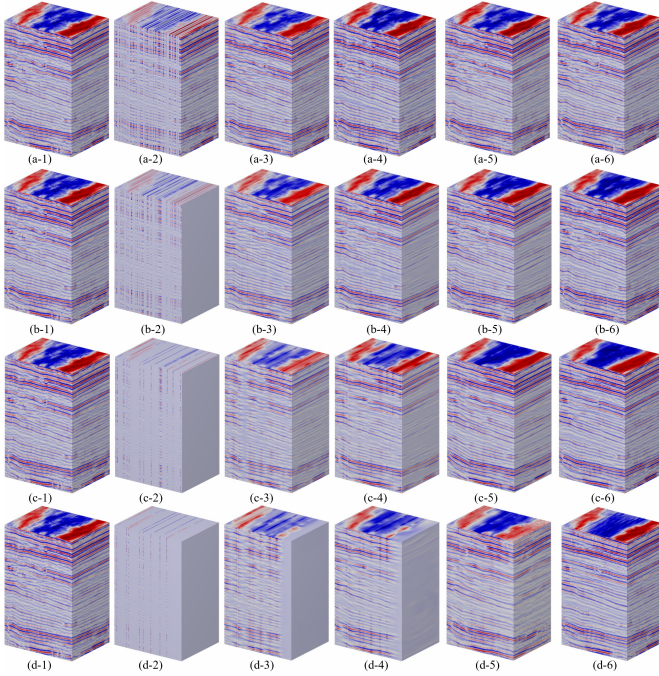


Fig. 5. New Zealand Parihaka. The cuboid size is $256 \times 160 \times 128$. (a-x), (b-x), (c-x), and (d-x) are the reconstruction results of each method with 50%, 75%, 90%, and 95% random discrete missing, respectively. (x-1), (x-2), (x-3), (x-4), (x-5) and (x-6) correspond to the original data, the missing data and the reconstruction results of Group-1 Group-2 Group-3 and Group-4, respectively.

B. Continuous Missing

Next, we compare the performance of the four methods in the continuous missing case. It should be noted that the best repair record for missing continuous seismic traces is currently by Yu et al. [2]. They interpolated 30% of the missing continuous traces of the 128×128 2-D seismic image with an interpolated area of 128×38 .

TABLE II
SSIM AND PSNR

	Missing Ratio	50%	75%	90%	95%
SSIM	Group-1	0.9661	0.9377	0.8734	0.7592
	Group-2	0.9882	0.9401	0.8793	0.7792
	Group-3	0.9661	0.9679	0.9184	0.8460
	Group-4	0.9875	0.9668	0.9233	0.8659
PSNR	Group-1	31.53	29.88	25.85	19.13
	Group-2	36.72	31.21	26.69	21.96
	Group-3	36.69	32.19	28.50	24.37
	Group-4	36.65	32.41	29.17	25.1

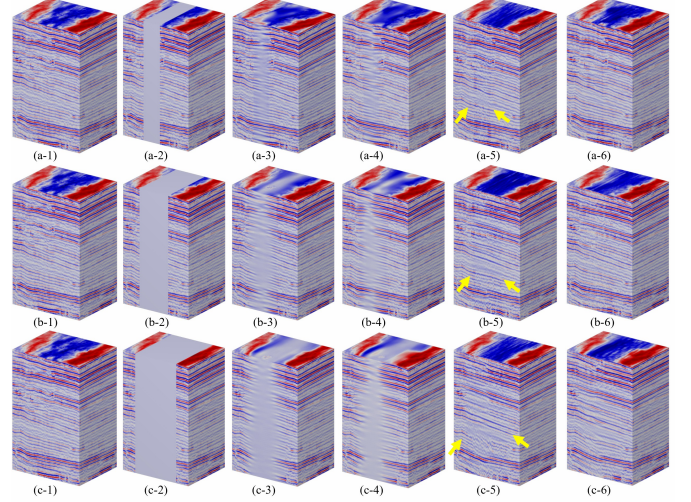


Fig. 6. New Zealand Parihaka. (a-x), (b-x), and (c-x) are the reconstruction results of each method with 40, 70, and 100 consecutive missing, respectively. (x-1), (x-2), (x-3), (x-4), (x-5) and (x-6) correspond to the original data, the missing data and the reconstruction results of Group-1 Group-2 Group-3 and Group-4, respectively.

Fig. 6 illustrates three consecutive missing, 40, 70, and 100 traces. In the case of consecutive missing cases, Group-1 and Group-2 show unsatisfactory reconstructions with significant voids, and it can be observed that the regression method is only an extension of the data in the neighbourhood of the missing site and is limited in scope. The MDA GAN-based approach performs the reconstruction task well in the continuous missing case, but the reconstruction of the missing parts using L_1 loss has pixel distortion, a phenomenon also found in Oliveira's work [17], which we speculate is caused by unsmoothed gradients during training, and as discussed above, the L_1 loss does not reflect the distance of the output from the label under the Tanh activation function, resulting in distortion of some pixels in the model output, some of the trace discontinuities in Fig. 5 (d-5) are also caused by this respect. Therefore MDA GAN using TCE loss provides more consistent and smoother results.

C. Feature Splicing Module

We have initially verified the role of the FSM module with Fig 4. Noteworthy is the effect of FSM on the quantitative metrics (Group-1 and Group-2). The impact of the FSM on the interpolation performance is difficult for the human eye

TABLE III
SSIM AND PSNR

	Continuous Traces	40	70	100
SSIM	Group-1	0.9161	0.8455	0.7486
	Group-2	0.9409	0.8771	0.7871
	Group-3	0.9655	0.8829	0.8104
	Group-4	0.9689	0.9092	0.8333
PSNR	Group-1	25.11	23.67	23.75
	Group-2	28.66	26.55	21.92
	Group-3	33.60	29.17	24.22
	Group-4	34.07	29.44	25.01

to perceive in the qualitative results of Fig. 5 and Fig. 6, while the quantitative metrics of Tables II and III clearly show their differences. We calculate the SSIM map¹ from the interpolation results of Fig. 5 (a-3) and (a-4) with the original data respectively (Fig. 7 (a)), and the SSIM map can adequately reflect the spatial distribution of the differences between the two images.

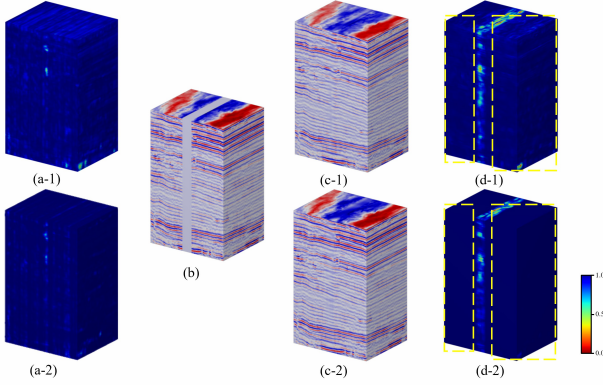


Fig. 7. (a-1) and (a-2) correspond to the SSIM maps obtained by comparing Group 1 and Group 2 with the original data in the 50% random discrete missing case, respectively. (b) is 20 consecutive missing, (c-1) and (c-2) are the reconstruction results of Group-1 and Group-2, respectively, and (d-1) and (d-2) are their SSIM maps.

In Fig. 7 (a) it is clearly reflected that the result without FSM has more differences compared to the original data. To reflect this disparity more clearly, we made the missing concentrated in the middle of the data (20 consecutive missing traces, Fig. 7 (b)), Fig. 7 (c) is the interpolation results, and Fig. 7 (d) is the result with the original SSIM map. Fig. 7 (d-1) has almost no difference between the unmissing part (yellow box) and the original map, while Fig. 7 (d-2) shows a significant difference.

This indicates that the FSM adaptively splices the features of the unmissing part of the input data with the generated features, whereas a network that does not use the FSM needs to reconstruct the complete data, so the unmissing part of the output differs significantly from the original data.

D. Hybrid Missing

In the above experiments, we tested up to 95% of random discrete missing and up to 100 consecutive missing traces. The

complexity of the cases we tested is well beyond the scope discussed in previous work, and promising results can still be obtained with MDA GAN. In this subsection, we hybridize the two types of missing to test the performance of the method in more complex cases. We tested this in the New Zealand Parihaka and Netherlands Offshore F3 surveys, both of which sampled at a total of $192 \times 384 \times 256$ grid points.

We set three consecutive 80-trace missing and 75% random discrete missing on inline, and two 80-trace missing and 75% missing on crossline, for a cumulative missing voxel of 99.4%. Since Group-1, Group-2 and Group-3 display unsatisfactory performance in the above experiments, only the results of MDA GAN are presented here.

Fig. 9 (a) displays the results of MDA GAN in Parihaka. The survey in Fig. 9 (a-2) has been disfigured and it is difficult for humans to imagine the original data based on this figure, but MDA GAN still recovered the survey by few priors in Fig. 9 (a-3), and the tilt direction of the reflection (arrow direction) is the same as the original data. The interpolation of this survey results in SSIM of 0.8021, PSNR of 26.06 compared with the original. Fig. 9 (b) displays the results of MDA GAN in F3. Similar to Parihaka, our method yielded promising results despite extreme difficulties, with the reconstructed SSIM of 0.7586 and PSNR of 25.39.

Although the reconstructions of both surveys show some flaws in timeline, the mixture the high proportion of random discrete missing and the large range of continuous missing is extremely challenging for the model, but from inline, crossline and SSIM, MDA GAN still obtains stable and reasonable reconstructions with only 0.6% prior.

E. Testing in Fault-rich Surveys

Interpolation of fault-rich surveys is very challenging, to the best of our knowledge, no work on interpolation in this case has been discussed. The reflection of faults is anomalous in seismic data, and the missing fault region means that information is lost, which is difficult to recover by conventional methods.

1) *Synthetic data*: We use Wu's publicly available synthetic fault seismic data as the test sample [39]. We compare the interpolation performance of Group-1, Group-2 and Group-4 for fault-rich surveys in Fig. 9. (a) is inline 75% missing, 75% missing is difficult for most of the algorithms. (b) is both inline and crossline 75% missing, totaling 92.9% missing. (c) is 50% missing inline, crossline and timeline combined, totaling 86.7% missing. (d) is 75% missing inline, crossline and timeline combined, totaling 98.2% missing. (e) is the continuous missing of 80 traces on inline.

In Fig. 11 (a), MDA GAN shows a great advantage when the deficiency is 75% in one direction. Although Group-1 and Group-2 completed the interpolation, the regression method has difficulty in restoring the details of the fault, which can be seen at the arrow in Fig. 11. MDA GAN provides a better restoration of the details of the fault. In Fig. 11 (b), the complex discrete missing in both directions makes the Group-1 and Group-2 show obvious missing traces and wrong interpolation. And the MDA GAN still does a excellent work

¹skimage. [Online]. Available: <https://scikit-image.org>

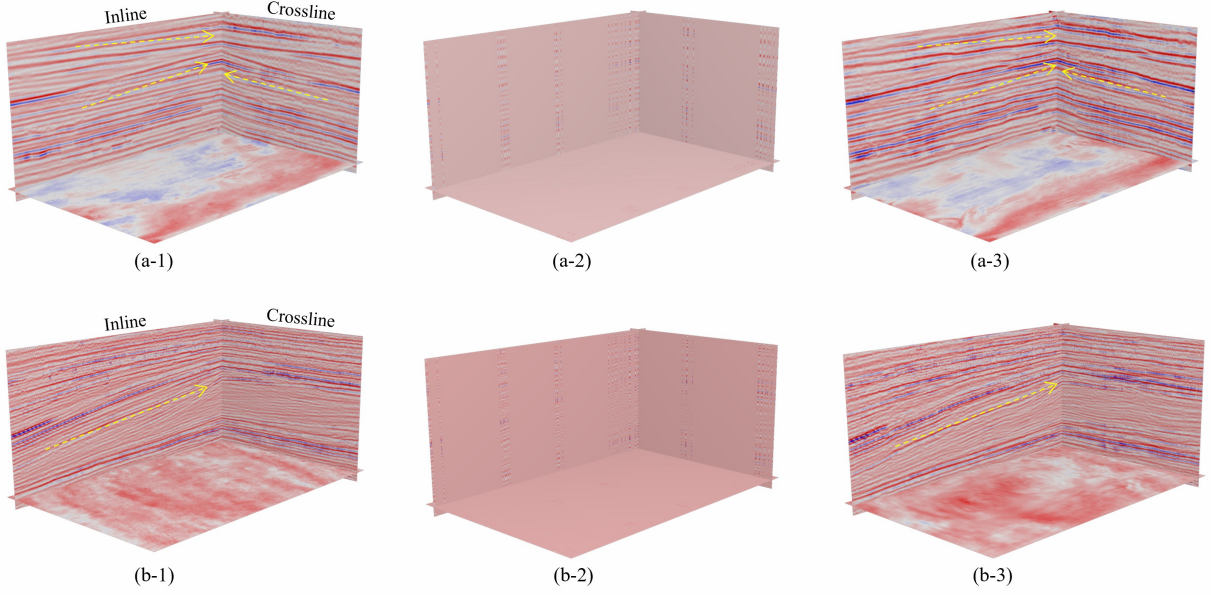


Fig. 8. New Zealand Parihaka and Netherlands Offshore F3. The cuboid size is $192 \times 384 \times 256$, (a-x) is New Zealand Parihaka, (b-x) is Netherlands Offshore F3. (x-1) is the original data, (x-2) is the missing data, and (x-3) is the reconstruction result of MDA GAN.

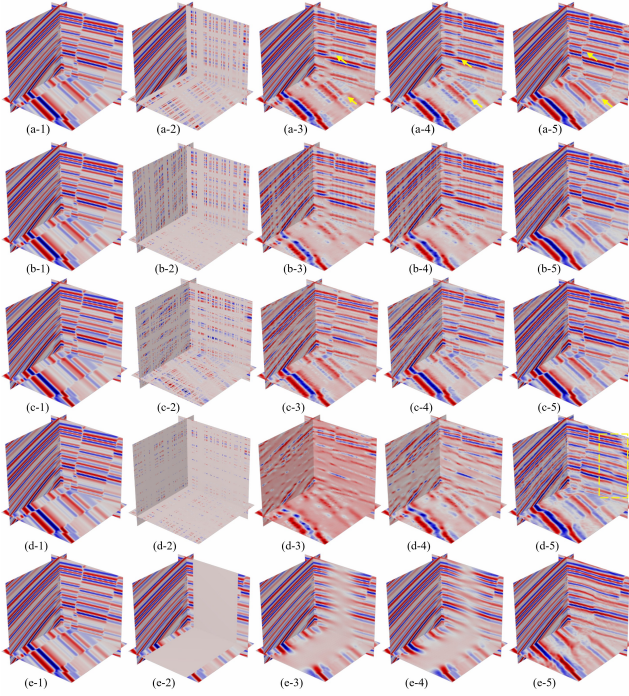


Fig. 9. Synthetic fault data. The cuboid size is $128 \times 128 \times 128$. (a-x), (b-x), (c-x), (d-x), and (e-x) are the reconstruction results for 75% one direction random dispersion, 75% two direction random dispersion, 50% three direction random dispersion, 75% three direction random dispersion, and 80 consecutive trace missing, respectively. (x-1), (x-2), (x-3), (x-4) and (x-5) correspond to the original data, the missing data and the reconstruction results of Group-1 Group-2 and Group-4, respectively.

of delicate interpolation. In Fig. 11 (c) is a random deletion of 50% in each of the three directions, the results for Group-1 and Group-2 have obvious blurring and unnatural artefacts, and the MDA GAN outputs are much closer to the original

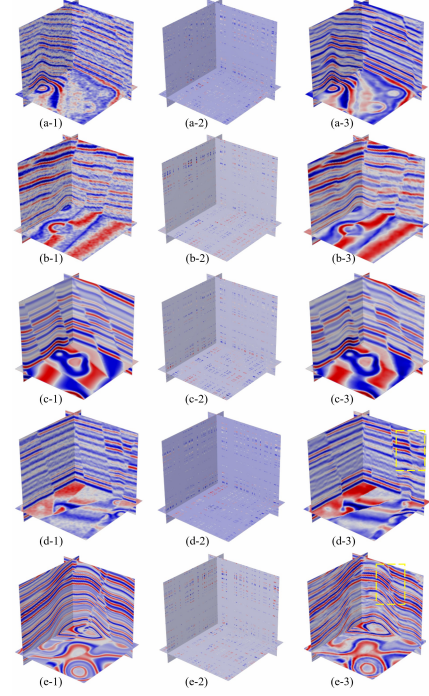


Fig. 10. Synthetic fault data. The cuboid size is $128 \times 128 \times 128$. (x-1), (x-2) and (x-3) are the original data, the missing data and the data after reconstruction by MDA GAN, respectively.

data. In Fig. 11 (d) three directions of 70% random discrete missing, the methods of Group-1 and Group-2 have lost their effect and our method accomplishes a promising interpolation, but the yellow box in (d-5) shows blurred faults.

In Fig. 11 (e), the continuous missing of 80 traces makes the data lose the fault information, and MDA GAN recovered the reflection of the seismic, but did not reconstruct the fault.

This indicates that our method can recover fault information when the missing region covers part of the fault or when the adjacent reflection have fracture characteristics, but when the fault is completely covered by continuous missing, MDA GAN can only recover the seismic reflections and cannot recover the fault.

To verify the generalizability of our method, we test more synthetic data in Fig. 12. Since in Fig. 11, the MDA GAN demonstrates promising performance in (a)-(c), and only (d) shows blurred faults in some regions, we test only the missing cases in 75% of each of the three directions, totaling 98.2% missing. In Fig. 12 of (a)-(c), MDA GAN not only recovers the original fault information, but also has a clearer reflection with some denoising effect compared with the original data. There are some blurred faults in the yellow boxes of (d) and (e). The primary factor is that the original fracture characteristics is unclear and the missing coincides with covering the critical cue regions of its faults, resulting in the blurred results obtained by MDA GAN.

2) *New Zealand Kerry*: To further validate the performance of our method, we test it in field fault-rich surveys. We tested New Zealand Kerry and intercepted the fault-rich areas of it, which sampled at a total of $272 \times 512 \times 192$ grid points.

In Fig. 12 displays the massive vertical faults of this survey, which are well defined and clear, and when the missing rate is 50% in three directions (86.7% in total, Fig. 12 (a-2)), the missing area covers some vertical faults, but our method is able to restore fault information based on adjacent reflections (Fig. 12 (a-3)), except for some continuous faults, for which our method almost restores the original data. In Fig. 12 (b-2) shows 75% missing in each of the three directions (98.2% in total), and most of the faults in this region are covered by the missing, making it very difficult to interpolate the field data. The arrow in In Fig. 12 (b-2) shows two consecutive missing, which completely cover the fault, resulting in the failure to complete the recovery of the fault at the position corresponding to (b-3). With a great percentage of missing, our method still recovers Kerry's reflection, but it is difficult to handle for some faults.

3) *Netherlands Offshore F3*: There are some fault-rich areas at the bottom of F3 survey. We tested Netherlands Offshore F3 and intercepted the fault-rich areas of it, which sampled at a total of $128 \times 512 \times 384$ grid points. Compared with Kerry, the fault-rich area of F3 has less obvious fracture characteristics of the reflection, which makes the reconstruction difficult.

Fig. 12 (a-2) shows 50% missing in each of the three directions (86.7% in total), and (a-3) shows the reconstruction results of MDA GAN. At the box, the method reconstructs the fault structure well and shows promising results for the multi-directional faults at the circles. While at (b-2) when the three-directional missing rate reaches 75% (98.2% in total), only reflections are reconstructed at these two locations, and most of the fault information is lost.

This demonstrates that a lower proportion of the missing MDA GAN can reconstruct its fault structure when the fracture characteristics of the reflection are not obvious, but when the proportion is too large the MDA GAN is overpowered and can only reconstruct its reflection.

Moreover, there are some salt bodies at the bottom of F3, which are anomalies like faults and are more challenging to reconstruct compared to conventional reflections, but compared to faults, the salt bodies are more extensive, and it is difficult to cover the salt bodies with random and discrete missing, so it is simpler to reconstruct than faults.

Fig. 13 displays the salt body region of F3. Fig. 13 (a-2) is 50% missing in three directions (86.7% in total), and humans can still observe the outline of the salt body. In (a-3) our method not only reconstructs the reflection at the salt body region, but restores the details of the salt body as well. Fig. 13 (b-2) is 75% missing in three directions (98.2% in total), the reflection at the salt body has been broken and the details are almost completely lost, and it is also difficult for humans to observe its presence, but MDA GAN still performs a promising reconstruction, and although its details at the arrows are slightly different, the reflection and the salt body have been excellent restored.

IV. CONCLUSION

Seismic interpolation and reconstruction in 3-D complex cases have rarely been mentioned in previous work. In this study, to cope with these cases, we propose the MDA GAN, which guarantees the consistency of feature distribution in each dimension with the original data through adversarial learning, so that reasonable results can be generated even in complex cases. Meanwhile, the FSM embedded in its generator can fully retain the information of the unmissing parts, and the TCE loss can ensure that the pixels are not distorted and the generated results are more continuous. In comparison with methods such as UNet, MDA GAN shows great advantages in both simple and complex missing, and also demonstrates the effectiveness of the FSM and TCE components in generating reasonable results, especially in extremely complex cases. Moreover, we have tested performance in surveys with fault-rich and salt bodies. In such data, for random discrete absences, our method can reconstruct their reflections and faults, but for large continuous missing areas, MDA GAN can only reconstruct their reflections. This work is the first to propose a 3-D GAN framework for seismic data interpolation and reconstruction, and to experiment and discuss it in the context of extreme complexities such as random discrete and continuous missing at high scales, as well as fault enrichment and salt body surveys, where the method gives promising results in all these extreme cases.

ACKNOWLEDGMENT

The authors are very indebted to the anonymous referees for their critical comments and suggestions for the improvement of this paper.

REFERENCES

- [1] J. Park, D. Yoon, S. J. Seol, and J. Byun, "Reconstruction of seismic field data with convolutional u-net considering the optimal training input data," in *SEG International Exposition and Annual Meeting*. OnePetro, 2019.
- [2] J. Yu and B. Wu, "Attention and hybrid loss guided deep learning for consecutively missing seismic data reconstruction," *IEEE Transactions on Geoscience and Remote Sensing*, 2021.

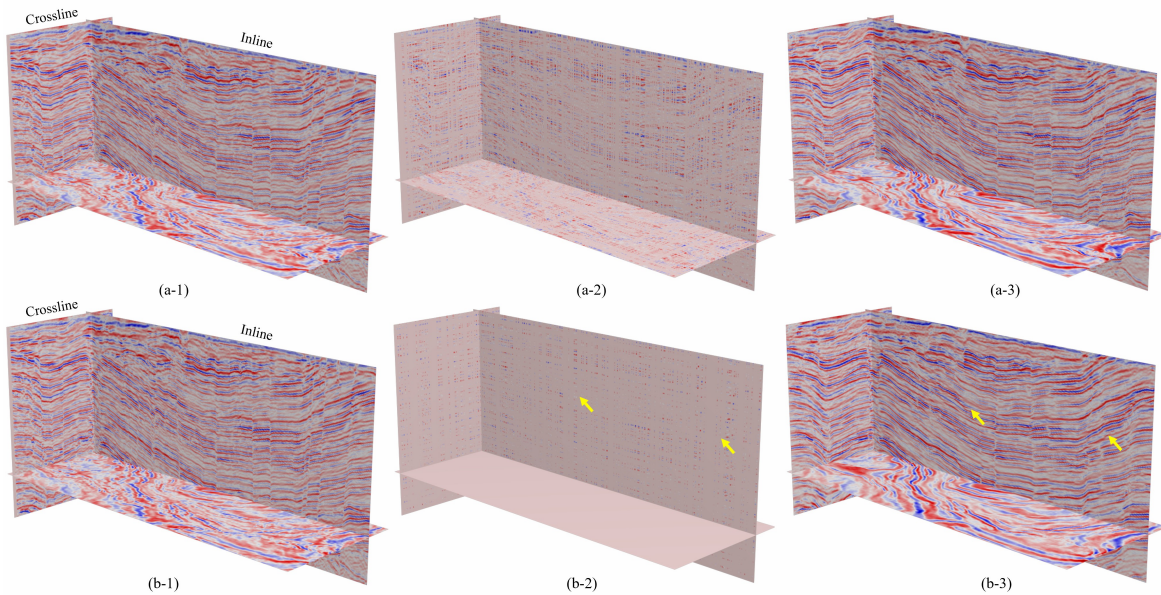


Fig. 11. New Zealand Kerry. The cuboid size is $272 \times 512 \times 192$, (x-1), (x-2) and (x-3) are the original data, the missing data and the data after reconstruction by MDA GAN, respectively. (a-x) is 50% missing in three directions and (b-x) is 75% missing in three directions.

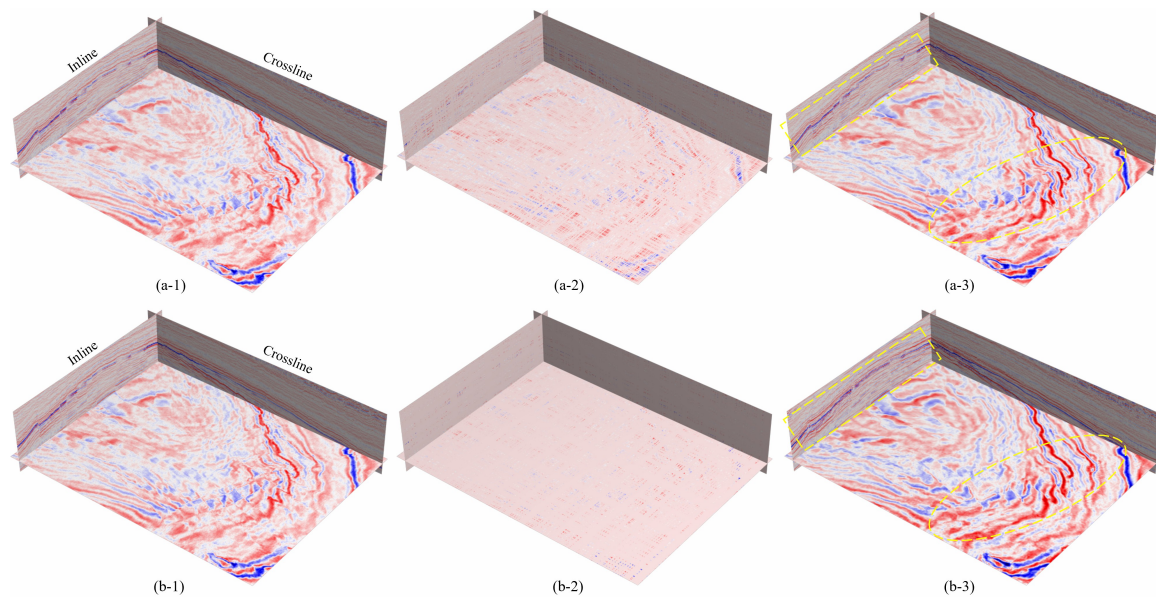


Fig. 12. Netherlands Offshore F3 (fault). The cuboid size is $128 \times 512 \times 384$, (x-1), (x-2) and (x-3) are the original data, the missing data and the data after reconstruction by MDA GAN, respectively. (a-x) is 50% missing in three directions and (b-x) is 75% missing in three directions.

- [3] F. J. Herrmann and G. Hennenfent, "Non-parametric seismic data recovery with curvelet frames," *Geophysical Journal International*, vol. 173, no. 1, pp. 233–248, 2008.
- [4] J. Ma, "Three-dimensional irregular seismic data reconstruction via low-rank matrix completion," *Geophysics*, vol. 78, no. 5, pp. V181–V192, 2013.
- [5] B. Wang, "An efficient pocs interpolation method in the frequency-space domain," *IEEE Geoscience and Remote Sensing Letters*, vol. 13, no. 9, pp. 1384–1387, 2016.
- [6] J. Gao, J. Cheng, and M. D. Sacchi, "Five-dimensional seismic reconstruction using parallel square matrix factorization," *IEEE Transactions on Geoscience and Remote Sensing*, vol. 55, no. 4, pp. 2124–2135, 2016.
- [7] W. Huang, R.-S. Wu, and R. Wang, "Damped dreamlet representation for exploration seismic data interpolation and denoising," *IEEE Transactions on Geoscience and Remote Sensing*, vol. 56, no. 6, pp. 3159–3172, 2018.
- [8] G. Liu, C. Li, Z. Guo, and Y. Rao, "Irregularly sampled seismic data reconstruction using multiscale multidirectional adaptive prediction-error filter," *IEEE Transactions on Geoscience and Remote Sensing*, vol. 57, no. 5, pp. 2909–2919, 2018.
- [9] W. Huang and J. Liu, "Robust seismic image interpolation with mathematical morphological constraint," *IEEE Transactions on Image Processing*, vol. 29, pp. 819–829, 2019.
- [10] M. Sacchi, S. Kaplan, and M. Naghizadeh, "Fx gabor seismic data reconstruction," in *71st EAGE Conference and Exhibition incorporating SPE EUROPEC 2009*. European Association of Geoscientists & Engineers, 2009, pp. cp-127.
- [11] B. Wang, N. Zhang, W. Lu, and J. Wang, "Deep-learning-based seismic data reconstruction: A preliminary result," *Geophysics*, vol. 84, no. 1, pp. V11–V20, 2019.
- [12] Y. Wang, B. Wang, N. Tu, and J. Geng, "Seismic trace interpolation for irregularly spatial sampled data using convolutional autoencoder," *Geophysics*, vol. 85, no. 2, pp. V119–V130, 2020.

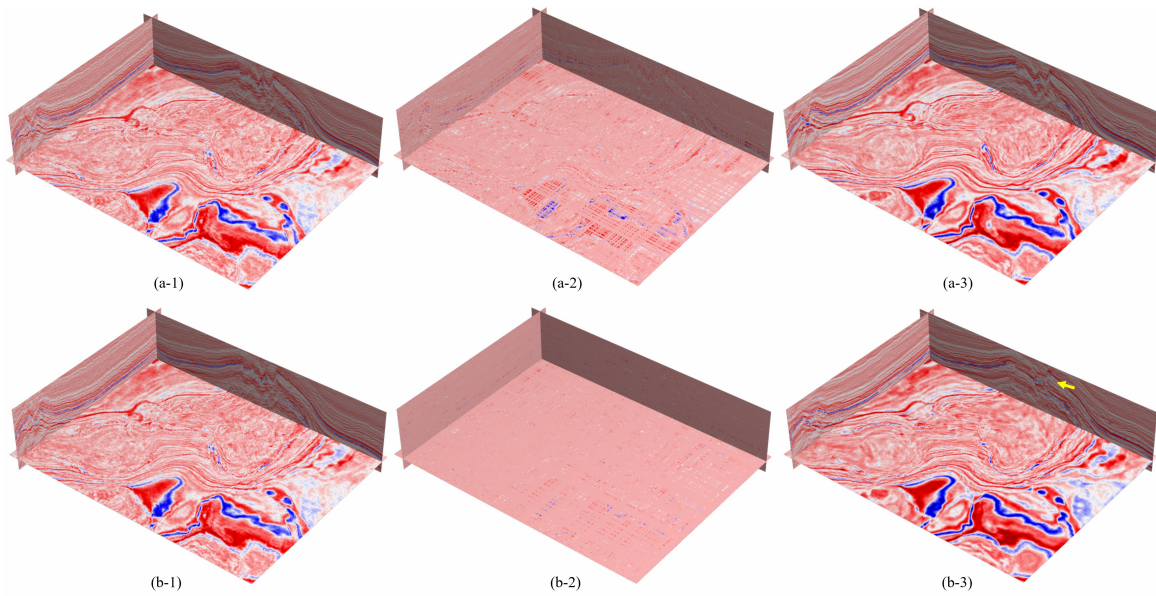


Fig. 13. Netherlands Offshore F3 (salt body). The cuboid size is $128 \times 512 \times 384$, (x-1), (x-2) and (x-3) are the original data, the missing data and the data after reconstruction by MDA GAN, respectively. (a-x) is 50% missing in three directions and (b-x) is 75% missing in three directions.

- [13] B. Wang, N. Zhang, W. Lu, P. Zhang, and J. Geng, "Seismic data interpolation using deep learning based residual networks," in *80th EAGE Conference and Exhibition 2018*, vol. 2018, no. 1. European Association of Geoscientists & Engineers, 2018, pp. 1–5.
- [14] T. He, B. Wu, and X. Zhu, "Seismic data consecutively missing trace interpolation based on multistage neural network training process," *IEEE Geoscience and Remote Sensing Letters*, vol. 19, pp. 1–5, 2021.
- [15] X. Li, B. Wu, X. Zhu, and H. Yang, "Consecutively missing seismic data interpolation based on coordinate attention unet," *IEEE Geoscience and Remote Sensing Letters*, vol. 19, pp. 1–5, 2021.
- [16] F. Qian, Z. Liu, Y. Wang, S. Liao, S. Pan, and G. Hu, "Dtac: Deep tensor autoencoder for 3-d seismic data interpolation," *IEEE Transactions on Geoscience and Remote Sensing*, 2021.
- [17] D. A. Oliveira, R. S. Ferreira, R. Silva, and E. V. Brazil, "Interpolating seismic data with conditional generative adversarial networks," *IEEE Geoscience and Remote Sensing Letters*, vol. 15, no. 12, pp. 1952–1956, 2018.
- [18] Q. Wei, X. Li, and M. Song, "De-aliased seismic data interpolation using conditional wasserstein generative adversarial networks," *Computers & Geosciences*, vol. 154, p. 104801, 2021.
- [19] H. Kaur, N. Pham, and S. Fomel, "Seismic data interpolation using cyclegan," in *SEG Technical Program Expanded Abstracts 2019*. Society of Exploration Geophysicists, 2019, pp. 2202–2206.
- [20] —, "Seismic data interpolation using deep learning with generative adversarial networks," *Geophysical Prospecting*, vol. 69, no. 2, pp. 307–326, 2021.
- [21] A. Newell, K. Yang, and J. Deng, "Stacked hourglass networks for human pose estimation," in *European conference on computer vision*. Springer, 2016, pp. 483–499.
- [22] V. Badrinarayanan, A. Kendall, and R. Cipolla, "Segnet: A deep convolutional encoder-decoder architecture for image segmentation," *IEEE transactions on pattern analysis and machine intelligence*, vol. 39, no. 12, pp. 2481–2495, 2017.
- [23] O. Ronneberger, P. Fischer, and T. Brox, "U-net: Convolutional networks for biomedical image segmentation," in *International Conference on Medical image computing and computer-assisted intervention*. Springer, 2015, pp. 234–241.
- [24] H. Noh, S. Hong, and B. Han, "Learning deconvolution network for semantic segmentation," in *Proceedings of the IEEE international conference on computer vision*, 2015, pp. 1520–1528.
- [25] A. Radford, L. Metz, and S. Chintala, "Unsupervised representation learning with deep convolutional generative adversarial networks," *arXiv preprint arXiv:1511.06434*, 2015.
- [26] D. Pathak, P. Krahenbuhl, J. Donahue, T. Darrell, and A. A. Efros, "Context encoders: Feature learning by inpainting," in *Proceedings of the IEEE conference on computer vision and pattern recognition*, 2016, pp. 2536–2544.
- [27] C. Zheng, T.-J. Cham, and J. Cai, "Pluralistic image completion," in *Proceedings of the IEEE/CVF Conference on Computer Vision and Pattern Recognition*, 2019, pp. 1438–1447.
- [28] Z. Yi, Q. Tang, S. Azizi, D. Jang, and Z. Xu, "Contextual residual aggregation for ultra high-resolution image inpainting," in *Proceedings of the IEEE/CVF Conference on Computer Vision and Pattern Recognition*, 2020, pp. 7508–7517.
- [29] Y. Zeng, Z. Lin, H. Lu, and V. M. Patel, "Cr-fill: Generative image inpainting with auxiliary contextual reconstruction," in *Proceedings of the IEEE/CVF International Conference on Computer Vision*, 2021, pp. 14 164–14 173.
- [30] I. Goodfellow, J. Pouget-Abadie, M. Mirza, B. Xu, D. Warde-Farley, S. Ozair, A. Courville, and Y. Bengio, "Generative adversarial nets," *Advances in neural information processing systems*, vol. 27, 2014.
- [31] K. Sun, B. Xiao, D. Liu, and J. Wang, "Deep high-resolution representation learning for human pose estimation," in *Proceedings of the IEEE/CVF Conference on Computer Vision and Pattern Recognition*, 2019, pp. 5693–5703.
- [32] J. Wang, K. Sun, T. Cheng, B. Jiang, C. Deng, Y. Zhao, D. Liu, Y. Mu, M. Tan, X. Wang *et al.*, "Deep high-resolution representation learning for visual recognition," *IEEE transactions on pattern analysis and machine intelligence*, 2020.
- [33] Y. Dou, K. Li, J. Zhu, T. Li, S. Tan, and Z. Huang, "Efficient training of 3d seismic image fault segmentation network under sparse labels by weakening anomaly annotation," *arXiv preprint arXiv:2110.05319*, 2021.
- [34] K. He, X. Zhang, S. Ren, and J. Sun, "Deep residual learning for image recognition," in *Proceedings of the IEEE conference on computer vision and pattern recognition*, 2016, pp. 770–778.
- [35] T. Miyato, T. Kataoka, M. Koyama, and Y. Yoshida, "Spectral normalization for generative adversarial networks," *arXiv preprint arXiv:1802.05957*, 2018.
- [36] D. P. Kingma and J. Ba, "Adam: A method for stochastic optimization," *arXiv preprint arXiv:1412.6980*, 2014.
- [37] M. Heusel, H. Ramsauer, T. Unterthiner, B. Nessler, and S. Hochreiter, "Gans trained by a two time-scale update rule converge to a local nash equilibrium," *Advances in neural information processing systems*, vol. 30, 2017.
- [38] Z. Wang, A. C. Bovik, H. R. Sheikh, and E. P. Simoncelli, "Image quality assessment: from error visibility to structural similarity," *IEEE transactions on image processing*, vol. 13, no. 4, pp. 600–612, 2004.
- [39] X. Wu, L. Liang, Y. Shi, and S. Fomel, "Faultseg3d: Using synthetic data sets to train an end-to-end convolutional neural network for 3d seismic fault segmentation," *Geophysics*, vol. 84, no. 3, pp. IM35–IM45, 2019.